THE JOURNAL OF PHYSICAL CHEMISTRY C

Article

Cite This: J. Phys. Chem. C 2019, 123, 19579−19587

pubs.acs.org/JPCC

Fabrication of Anisotropic Silver Nanoplatelets on the Surface of TiO_2 Fibers for Enhanced Photocatalysis of a Chemical Warfare Agent Simulant, Methyl Paraoxon

Published as part of The Journal of Physical Chemistry virtual special issue "Hai-Lung Dai Festschrift".

Danielle L. Kuhn,[†] Zachary Zander,[†] Ann M. Kulisiewicz,[†] S. M. Debow,[†] Connor Haffey,[†] Hui Fang,[‡] Xiang-Tian Kong,[§] Yuqin Qian,[⊥] Scott D. Walck,[∥] Alexander O. Govorov,[§] Yi Rao,[⊥] Hai-Lung Dai,[‡] and Brendan G. DeLacy*[,†]

[†]U.S. Army Combat Capabilities Development Command Chemical Biological Center, Research & Technology Directorate, Aberdeen Proving Ground, Maryland 21010, United States

[‡]Department of Chemistry, Temple University, Philadelphia, Pennsylvania 19122, United States

[§]Department of Physics and Astronomy, Ohio University, Athens, Ohio 45701, United States

[∥]Survice Engineering Company, U.S. Army Research Laboratory, Aberdeen Proving Ground, Maryland 21005, United States

[⊥]Department of Chemistry and Biochemistry, Utah State University, Logan, Utah 84322-0300, United States

Supporting Information

ABSTRACT: Among the world's most deadly toxins are a class of organophosphates that are used as chemical warfare agents (CWAs). It is imperative to continue to develop novel means for mitigation and protection against these chemical threats. Sensitizing the surface of metal oxide semiconductors with plasmonic nanoparticles for photocatalytic degradation of chemical threats has been a prominent area of research in recent years. Anisotropic silver nanoplateles were purposefully grown on the surface of TiO_2 fibers, in order to determine the impact of silver nanoparticle shape on (1) the generation of hot electrons by the silver, (2) the subsequent transfer of those electrons from the silver into the TiO_2, and (3) the photocatalytic behavior of the Ag−TiO_2 composite. To elucidate the charge injection properties of the composites, transient absorption experiments (pump−probe experiments) were undertaken. These involved pumping the composite samples with a range of discrete visible wavelengths and probing the composite within the intraband transitions of the TiO_2. As a complement to these experiments, the photocatalytic properties of the Ag−TiO_2 composite fibers were studied via the photocatalytic hydrolysis of methyl paraoxon, a chemical warfare agent simulant. This involved exposure of the methyl paraoxon to either red, green, blue, or white LED illumination. For both the transient absorption and photocatalytic experiments, maximum efficiency was observed for those scenarios in which the resonance of the silver platelets most closely matched the wavelength of incident radiation. Furthermore, the composite with silver nanoplatelets clearly outperformed its counterpart with silver nanospheres, in terms of both charge injection and photocatalytic behavior. We believe these results shall serve as a basis for future catalytic research in which the resonance of anisotropic plasmonic nanoparticles (in a given composite) shall be designed to match the wavelength of incident radiation.

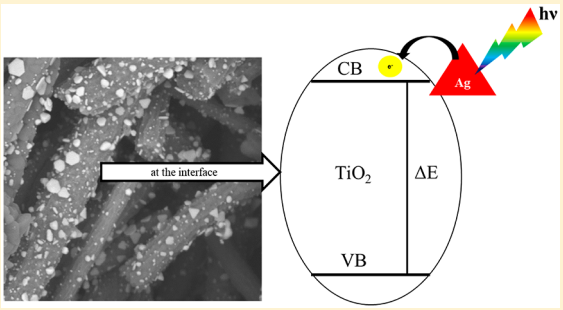

1. INTRODUCTION

Sensitizing the surface of metal oxide semiconductors with plasmonic metal nanoparticles has been a prominent area of research in recent years.[1,2] Several research groups have explored the use of gold or silver nanoparticles on the surface of metal oxides, such as titanium dioxide (TiO_2) and zinc oxide (ZnO), as a means of enhancing visible photocatalysis and solar energy conversion.[3,4] The presence of plasmonic nanoparticles on the surface of metal oxides provides several advantages. First, metal oxides such as TiO_2 have wide band gap energies which generate absorption primarily in the UV region. The inclusion of plasmonic nanoparticles on the surface of these metal oxides provides a means of extending the absorption of the plasmonic/metal-oxide nanocomposite from the UV into the visible region. The tunable nature of the surface plasmon resonance (SPR) in the visible region, via changes in the particle size and shape of the metal nanoparticle, is the driving force behind its use in improving

Received: May 6, 2019
Revised: July 22, 2019
Published: July 23, 2019

DOI: 10.1021/acs.jpcc.9b04026
J. Phys. Chem. C 2019, 123, 19579−19587

Scheme 1. Hydrolysis Mechanism of Dimethyl 4-nitrophenyl Phosphate (Methyl Paraoxon), a Chemical Analog of Phosphate Nerve Agents[a]

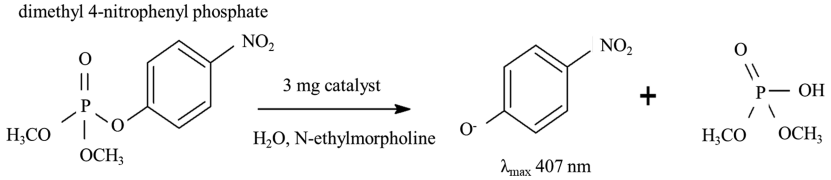

[a]For the premises of this manuscript, 3 mg of TiO_2 as prepared, spherical Ag−TiO_2, and anisotropic Ag−TiO_2 will be used as the catalyst.

visible light harvesting in the plasmonic/metal−oxide nanocomposites.[5−9]

A second distinct advantage of functionalizing metal-oxide semiconductors with plasmonic nanoparticles is the enhancement of photogenerated charge separation across the metal−semiconductor interface. This so-called hot electron injection process is one in which the photoexcited plasmon first decays into a hot electron−hole pair within the metal. The hot electron from the metal then decays into the conduction band of an adjacent semiconductor, providing charge separation at the Schottky barrier, which is formed at the metal−semiconductor interface.[10,11] The electron injection dynamics at the metal−semiconductor surface interface may be studied using transient absorption spectroscopy.[12,1,13−16] This is achieved by pumping the sample with a pulsed visible laser to generate hot electron within the metal, and then by probing the sample with an infrared laser pulse to monitor the absorption of the electron within the intraband transitions of the semiconductor's conduction band. The absorption of the probe pulse as a function of time therefore reveals the rate of injection of hot carrier from the metal to the semiconductor, as well as their decay. The choice of material and shape of plasmonic metal can be crucial for creation of large numbers of hot plasmonic electrons, which can be used in catalysis.[17−19] The shape of a nanocrystal is another crucial factor. It has been shown that the hot spots in a nanocrystal generate nonthermal (hot) electrons very efficiently.[17,18,15,16] In particular, the cubic and disk-like shapes exhibit high field amplification factors near the edges of a nanocrystal and, therefore, these shapes should be able to generate large numbers of hot electrons.[17,15] In that respect, choosing to decorate semiconductor with a nanocrystal that exhibits high field amplification is a plausible approach for generating hot electrons at or near the surface of the semiconductor.[17,16,18]

Photocatalytic degradation encompasses a variety of reactions including organic synthesis, photoreduction, hydrogen transfer, water detoxification, and gaseous pollutant removal.[20] TiO_2 is one particular photocatalytic material that has demonstrated its utility in the degradation of organic pollutants and other chemical threats. However, limitations of TiO_2 are due to its inherent band gap, which only allows this material to absorb in the ultraviolet region and a portion of the visible region. More specifically, TiO_2's band gap energy is limited to the use of only 5% of the total irradiation from natural sunlight.[21] There have been many efforts to functionalize the surface of metal oxide semiconductors with plasmonic nanoparticles, in order to overcome the limiting factors identified for photocatalysis. This has been possible through the introduction of gold or silver nanoparticles on the surface of the semiconductor. The growth of gold or silver nanoparticles typically involves exposing the semiconductor to a gold ($HAuCl_4$) or a silver ($AgNO_3$) salt in solution, respectively.[22−25] A reducing agent (e.g., $NaBH_4$) is subsequently used to convert the cationic form of the metal to its solid state. In contrast to the nanoparticle growth approach, premade gold or silver nanoparticles may be covalently attached to the surface of semiconductor materials using coupling agents such as silanes, thiols, or ss-DNA.[26−32] Regardless of how the plasmonic particles are deposited onto the surface of the semiconductor, i.e., via growth or covalent attachment, a *spherical* shape has been the primary nanoparticle geometry that has been explored in the deposition of metal nanoparticles on the surface of semiconductor materials.

In this study, we report the enhancement of TiO_2 photocatalytic behavior by decorating the surface of TiO_2 fibers with *anisotropic* silver nanoparticles and tuning the resonant wavelength to the source of irradiation. Anisotropic shapes of silver are particularly attractive for tuning and maximizing absorption in the visible region, due to the exceedingly high extinctions that are predicted in the literature.[33] The impact of nanoparticle geometry on plasmonic resonance and extinction has been, and continues to be, a well-studied area of research.[34−36] However, the impact of plasmonic nanoparticle geometry and anisotropy, and the associated plasmonic resonance, on the injection of hot electrons into an adjacent semiconductor for enhanced photocatalytic degradation has not been a focal point of research studies to date. To this end, we intentionally grew anisotropic, silver nanoplatelets on the surface of TiO_2 fibers. The photocatalytic properties of the Ag−TiO_2 composite fibers were studied via the photocatalytic hydrolysis of methyl paraoxon, a chemical warfare agent simulant. More specifically, the photocatalytic behavior of methyl paraoxon was determined under blue, green, and red LED illumination. The purpose of this approach was to elucidate the impact of matching (or mismatching) the wavelength of radiation with the resonance wavelength of the silver nanoplatelets on the overall catalytic behavior of the system. A general reaction mechanism for the hydrolysis of methyl paraoxon is provided in Scheme 1.

Methyl paraoxon is a benign simulant that has been studied in the literature for the more toxic class of organophosphate chemical agents, which are among the world's most deadly toxins.[37] Currently, employed as chemical warfare agents, phosphate esters have the ability to rapidly inhibit acetocholinesterase, a critical enzyme for nerve synapses to function properly, which ultimately leads to death.[38] Destruction of these CWAs is imperative. Currently, CWA degradation techniques include incineration, water hydrolysis followed by biotreatment, and water hydrolysis followed by supercritical water oxidation.[39,40] Drawbacks to these techniques include the selectivity of the analyte, degradation of the enzyme over lengthy treatment time, and lack of practicality.

DOI: 10.1021/acs.jpcc.9b04026
J. Phys. Chem. C 2019, 123, 19579−19587

As a complement to the photocatalytic study described above, transient absorption spectroscopy was also used to probe the electron injection process of the Ag−TiO_2 composite, i.e., to study the absorption of light by the silver nanoplatelets, the subsequent generation of hot electrons, and the transfer of those electrons from the silver into the TiO_2. Specifically, this involved pumping the Ag−TiO_2 composite at 400 nm wavelength and subsequently probing at 5260 nm (1900 cm^{-1}), in order to observe the injection of hot electrons into the intraband transitions of the TiO_2. Additionally, visible pump-visible probe experiments were undertaken at various "pump" wavelengths (515, 713, 742, 790, and 825 nm) in order to determine the impact of incident radiation wavelength on the generation of hot electrons by the silver nanoplatelets. In short, our overall goal in this study was to determine if the presence of anisotropic silver on the surface of TiO_2 fibers could enhance the injection of charge into the TiO_2, thereby enhancing the photocatalytic ability of the composite to degrade methyl paraoxon. More specifically, our goal was to determine how catalysis and free carrier generation were impacted by matching the resonance wavelength of the silver nanoplatelets with the wavelength of irradiation.

2. MATERIALS

Polyvinylpyrrolidone (M_w= 29 000), poly(methyl methacrylate) (M_w = 996 000), chloroform ($CHCl_3$), silver nitrate ($AgNO_3$), *N*,*N*-dimethylformamide (DMF), titanium isopropoxide (TTiP), dimethyl 4-nitrophenyl phosphate (DMNP or methyl paraoxon), *N*-ethyl morpholine, and sodium hydroxide pellets (NaOH) were purchased from Sigma-Aldrich, Alfa Aesar, and Fisher Scientific and used without any further purification. Deionized water of 18.2 MΩ·cm resistivity, obtained from a Millipore Direct-Q 5 system, was used in all experiments.

3. EXPERIMENTAL SECTION

3.1. Synthesis of TiO_2 Nanofibers. Electropsun TiO_2 nanofibers were fabricated using sol−gel synthesis and electrospinning followed by a thermal treatment. Procedures were reproduced from Liu et.al.[41] A 320 mg sample of poly(methyl methacrylate) (PMMA) was dissolved in 2 mL of chloroform and allowed to stir until the polymer was dissolved. Then, 0.67 mL of titanium isopropoxide (TTiP) was added dropwise to the polymer solution, which was allowed to stir for an additional 30 min. Next, 2 mL of dimethyl formamide (DMF) were added to the solution in order to increase the dielectric constant of the solution. The solution was then stirred for an additional 2 h prior to electrospinning. Electrospinning was achieved using an MTI Corporation benchtop electrospinning and electrospraying unit (Model HO-NFES-040-B). The sol−gel solution was added to a syringe, and the needle was placed 8 cm from the collector. The rotating mandrel collector was allowed to spin at 400 rpm. The syringe pump was set to 0.15 mL/min, and 8 kV was applied to the needle. The resulting composite nanofibers were allowed to stand for 24 h at room temperature under ambient conditions. This allowed for the hydrolysis of TTiP to $Ti(OH)_4$ and subsequent condensation to amorphous TiO_2 prior to thermal treatment.[42] The fibers were then collected and calcined in a Thermo Scientific Lindberg Blue M Mini-Mite Tiber Furnace (16 Pt: 120 V) at 400 °C for 4 h under atmospheric conditions.

3.2. Base Treatment of Electrospun TiO_2 Nanofibers. In order to promote the growth of anisotropic silver nanoplatelets on the surface of the electropsun nanofibers, 100 mg of TiO_2 was suspended in a 0.05 M NaOH solution and stirred continuously for 3 h. The resulting mixture was centrifuged and washed with DI water three times and then dried overnight in an oven at 100 °C.

3.3. Growth of Ag on the Surface of TiO_2. Ag−TiO_2 nanocomposites were synthesized using a modified polyol method from Su et al.[43] The solvothermal synthesis included 200 mg of PVP, 17 mg of $AgNO_3$, and 15 mg of TiO_2 nanofibers dissolved in 20 mL of DMF. The solution was placed into a three-neck round-bottom flask and stirred continuously. The contents of the flask were refluxed at 160 °C for 2 h. The DMF played a dual role of solvent and reducing agent for the Ag^+ ions to Ag. The previous exposure of the titania to a high pH was pertinent to nonspherical Ag growth at the fiber surface, while PVP was used as a stabilizing agent. The resulting solution was washed with deionized water and centrifuged; this was repeated three times until the supernatant solution was clear in color. The remaining solid was dried overnight at 100 °C. This method was used in the synthesis of Ag on both the surface of the base-treated TiO_2 and untreated TiO_2 nanofibers. To ensure PVP was no longer present in the sample, TGA was performed, and the results can be seen in the Supporting Information, Figure S5.[44]

3.4. Photocatalytic Degradation of Methyl Paraoxon. All degradation experiments were carried out at room temperature. Reactions were done in the presence of white, blue (475 nm), green (520−530 nm), and red (640 nm) LEDs. The LED spectra of the light sources can be seen in Figure S6. Simultaneously, the reaction was performed without incident irradiation, i.e., in a dark environment. A 3 mg sample of Ag−TiO_2 was introduced to an aqueous solution of *N*-ethyl morpholine (1 mL). The mixture was stirred continuously for 30 min to allow for adsorption desorption equilibrium. To the dispersed suspension was introduced 4 μL of methyl paraoxon (5.2 mg, 0.021 mmol) to the suspension. Then 10 μL aliquots were extracted through the course of the experiment at various time intervals (1, 5, 10, 15, 20, 25, 30, 60, and 120 min). Aliquots were diluted to 5 mL with 0.45 M aqueous *N*-ethyl morpholine and measured using UV−vis spectroscopy. *P*-Nitrophenoxide was monitored via UV−vis spectroscopy due to its absorbance at 407 nm. Standard control reactions were performed under the same conditions

3.5. Characterization and Associated Instrumentation. Powder X-ray diffraction (XRD) patterns of the nanofibers were recorded on a Panalytical X'Pert Pro diffractometer with Xcelerator, using Cu Kα radiation (λ = 1.5406 Å) at 45 kV and 40 mA. Scanning electron microscopy (SEM) images were obtained using a Hitachi S-4700 Field Emission SEM. Transmission electron microscopy (TEM) specimens were prepared via the nanoparticle suspension technique by dispersing the sample powders in ethanol and casting on holey carbon support films purchased from Ted Pella, Inc. The samples were examined using a JEOL 2100F TEM operated at 200 keV (JEOL USA, Inc.) in bright field (BF) and scanning transmission electron microscopy (STEM) BF and high angle annular dark field (HAADF) modes. TEM-BF images were acquired using Digital Micrograph and an Orius digital camera (Gatan, Inc.). STEM images were acquired using Digiscan and a model 806 HAADF STEM Detector (Gatan, Inc.) having a collection angle range of 48 to

DOI: 10.1021/acs.jpcc.9b04026
J. Phys. Chem. C 2019, 123, 19579−19587

144 mrad. Elemental analyses were performed using X-ray energy-dispersive spectra (XEDS) using an Octane Elite T windowless detector with the TEAM Analysis software (EDAX Inc.). Elemental X-ray maps were derived from spectrum images acquired with the EDAX system in the STEM mode and postprocessed using a multivariate statistical analysis technique with the Automated eXpert Spectral Image Analysis (AXSIA) toolbox. Photocatalysis experiments were performed using CREE XP solderless LEDs (RapidLED) mounted onto a u-shaped aluminum setup using screws. Thermal grease was applied behind the LEDs to reduce heat buildup during the course of the reaction that could affect the integrity of the light source. The setup was powered by a Mean Well LPC-35−700 constant current driver. The thermogravimetric analyses were performed on a TGA Q500 analyzer in a flow of 10 mL/min N_2 with a heating rate of 10 °C/min from 25 to 700 °C. Elemental analysis was performed with X-ray photoelectron spectroscopy (XPS) in an ultrahigh vacuum chamber. The XPS (PHOIBOS HV series) was equipped with a dual-anode (Mg and Al) X-ray source (DAR 400, Omicron Nanotechnology) and utilized a Z translation stage with 5° $x-y$ tilt for alignment with the sample. Detection of photoelectrons was achieved with an Omicron Sphera hemispherical analyzer with a five-channel detector mounted at a 45° angle relative to the X-ray source. The sample was outgassed within the load lock overnight to prevent increase in overall pressure in the main chamber.

3.6. Visible Pump- IR Probe Experiments. The experimental setup for the visible pump-transient IR probe experiments was described in our previous work.[45] Briefly, a regenerative-amplified Ti:Sapphire laser system (Quantronix, 100 fs), operating at 800 nm and 1 kHz repetition rate, was used for the experiments. A typical output power of the laser was 2.5 W. Then 40% of the 800 nm output was frequency doubled in a BBO crystal to generate a pump pulse of 400 nm with a pulse energy of 3 μJ. The remaining 60% of the output laser pulse was used to pump an IR Optical Parametric Amplifier (Quantronix, Palitra-FS) to produce an IR pulse of 5260 nm (1900 cm^{-1}) with a pulse energy of 1.5 μJ. The IR beam was attenuated by more than 1000 times before the samples. The IR probe was detected by a liquid nitrogen cooled HgCdTe detector (Judson J15D14-M204B-S01M-60-D31316), followed by an amplifier. The pump pulse was modulated by a chopper (New Focus Model 3501) at 500 Hz. The amplified IR signal from the detector was sent to a lock-in amplifier (Stanford Research, SR830). The digitized outputs were processed and recorded by a homemade Labview program. The instrumentation response function for the transient IR was 300 fs. The samples of TiO_2 and Ag−TiO_2 powders were pressed into thin slices, respectively. A typical thickness of the samples is around 100 μm for the transient IR absorption measurements.

3.7. Visible Pump-Visible Probe Experiments. A single-unit integrated femtosecond laser system (PHAROS, Light Conversion) with a seed oscillator was used in our experiments. The pulse duration is about 290 fs with 100 kHz repetition rate and a center wavelength at 1030 nm. The output power of the laser was 2.0 W in the experiments. 70% of the 1030 nm output was either frequency doubled in a BBO crystal to generate a pump pulse of 515 nm or directed toward an optical parametric amplifier (OPA) to generate different pump wavelengths including 713, 742, 790, and 825 nm. The remaining 30% of the output laser pulse was focused onto a YAG crystal plate to generate white light supercontinuum as a probe light. For these visible pump and visible probe experiments, the samples were probed dynamically from 500−1000 nm. The probe and pump light beams were focused and overlapped on the sample. Transmitted probe light was detected by a detection system. A charge coupled device (CCD) detection system (AvaSpec-ULS2048CL-EVO, Avantes) was used to obtain the signals. The pump pulse was modulated by an optical chopper (Model 3501, New Focus) at 500 Hz. The CCD sampling rate was synchronized with the chopper. The digitized outputs were processed and recorded by a homemade LabView program.

4. ELECTROMAGNETIC COMPUTATION MODELING OF AG−TIO_2 COMPOSITE

The optical extinction of the Ag nanoplatelets on TiO_2 fibers was numerically investigated by solving the wave equation of the electric field with the finite element solver in the RF module in the COMSOL software. In the simulations, the Ag nanoplatelets were described as short cylinders with rounded edges, whose typical thickness and diameter were estimated from the TEM images of the Ag−TiO_2 composite. The permittivity of Ag was taken from the literature.[46] To make simple, but reliable estimates for the extinctions, we used the effective medium approach to describe the dielectric environment of the medium surrounding the Ag nanoplatelets: The permittivity of the environmental medium was estimated by $\varepsilon_{eff} = f\varepsilon_{titania} + (1 - f)\varepsilon_{water}$, since the plasmonic resonances of the Ag nanoplatelets are influenced by both the TiO_2 fibers and the water solution. Given that $\varepsilon_{titania} = 6.8$, $\varepsilon_{water} = 1.8$, and taking $f = {}^1/_3$, we used a dispersionless permittivity of $\varepsilon_{eff} = 3.45$ for the environmental solvent. In other words, our choice of the materials fractions in ε_{eff}: $f = {}^1/_3$ and $1 - f = {}^2/_3$. We assumed that water contributes more to the effective dielectric constant of the matrix than the TiO_2 support, since the Ag−TiO_2 interface appears only below the Ag-nanocrystals, whereas the Ag-water interface is more extended and occupies the upper surface and the sides of the nanocrystal. The COMSOL simulation was performed in a spherical space with the radius of 400 nm and the Ag nanoplatelet was placed in the center. The truncated simulation space was surrounded by a perfect matched layer (100 nm) to absorb the outgoing light and prevent any back reflection. The continuity boundary condition was applied to the interface of Ag and the environmental medium, which guaranteed the continuities of tangential electric and magnetic fields components. The incident light beams were linearly polarized plane waves. The extinction of light was calculated as a combination of absorption and scattering of light, and then averaged over the three main polarization directions ($\mathbf{EP}\hat{x}$, $\mathbf{EP}\hat{y}$, $\mathbf{EP}\hat{z}$).

5. RESULTS AND DISCUSSION

Figure 1 provides a scanning electron microscopy image (SEM) of the as synthesized TiO_2 nanofibers. These fibers had no further treatment after their preparation and will be used as the baseline for the photocatalytic study.

The electrospinning process used to fabricate TiO_2 yielded nanofibers with an average diameter of 688 ± 32 nm and major dimensions on the order of tens of micrometers and greater.

TEM imaging was performed on all Ag−TiO_2 composite nanofibers, as shown in Figure 2. This was done to confirm and

DOI: 10.1021/acs.jpcc.9b04026
J. Phys. Chem. C 2019, 123, 19579−19587

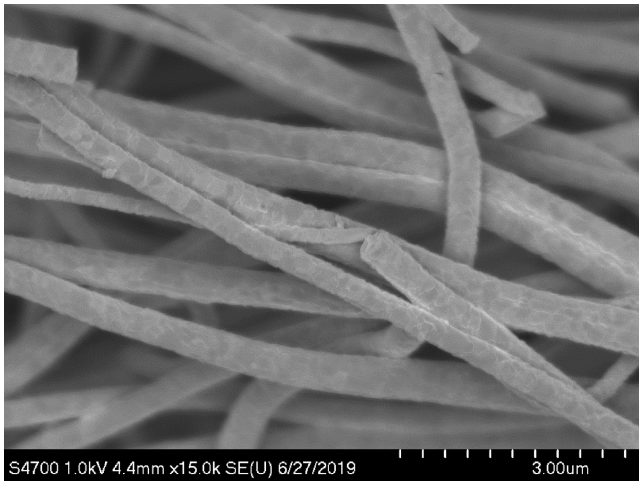

Figure 1. SEM image of raw TiO_2 nanofibers: i.e., untreated/no Ag. Average diameters are 688 ± 32 nm, and major dimensions are on the order of tens of micrometers and greater.

characterize the size and shape of both the platelet and spherical Ag on the surface of the TiO_2 nanofiber.

The untreated TiO_2 fibers, i.e., no exposure to base, clearly resulted in the growth of numerous spherical silver nanoparticles on the fiber surface, as shown in Figure 2d–f. For the case in which the TiO_2 fibers were exposed to basic conditions prior to silver growth, the TEM image clearly depicts the presence of numerous faceted platelet shapes, as demonstrated in Figure 2a–c. These observations were consistent with previous studies in which exposure of TiO_2 nanoparticles to a highly basic environment (pH > 11) prior to Ag deposition promoted the growth of anisotropic silver on the surface of TiO_2.[47−49] HRTEM was also used to demonstrate that no oxidation was present in the both the spherical Ag−TiO_2 and platelet Ag−TiO_2 geometry, Figure S9. Further images are included in the Supporting Information to validate that none of the Ag moieties were rod shaped and in fact were platelets on edge, Figure S7.

To understand the spectral properties of silver nanoplatelets, the extinction cross-section spectra of the nanoplatelets were calculated using the finite element method (COMSOL software). These computational results are provided in Figure 3. The nanoplatelets were modeled as Ag nanodisks with thickness of 15 nm, whose edges were rounded by a 5 nm radius. The nanodisks diameters were varied (40−75 nm) in the calculations to describe the dispersion of the major dimension of the synthesized nanoplatelets. Figure 3 clearly reveals that as the major dimension of the platelet increases, the main resonance of the platelet is red-shifted, and the magnitude of the extinction peaks increases in the visible spectral interval. Compared with the experimental extinction spectra of the silver nanoplatelets on TiO_2 fibers, which were superimposed onto the calculated spectra, it may be concluded

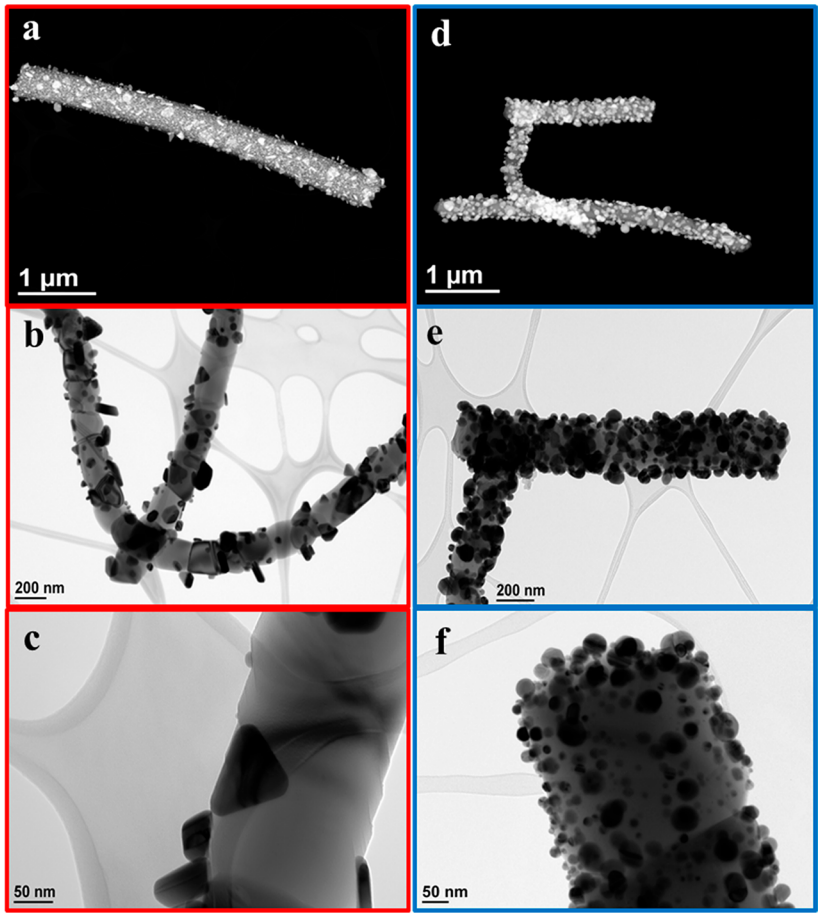

Figure 2. TEM images of platelet Ag−TiO_2 nanofibers (a−c) and spherical Ag−TiO_2 nanofibers (d−f). Images a and d are STEM-HAADF images, and images b, c, e, and f are TEM-BF images.

DOI: 10.1021/acs.jpcc.9b04026
J. Phys. Chem. C 2019, 123, 19579−19587

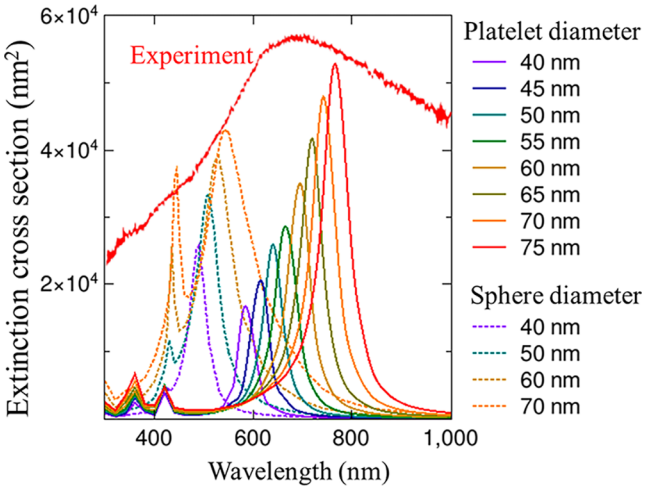

Figure 3. Calculated extinction cross-section spectra of silver nanoplatelets. The computed extinction spectra belong to nanoplatelets with major dimensions of 40−75 nm and nanosphere with 40−70 nm dimensions. A thickness of 15 nm and a rounded edge of 5 nm were assumed for the nanoplatelets. The red curve corresponds to the experimental spectrum of silver nanoplatelets on the surface of TiO_2 fibers.

that a distribution of silver platelets, varying in size, are present on the surface of the TiO_2 fibers. This conclusion is also consistent with the TEM image provided in Figure 2B.

In order to confirm the crystal structure of both the TiO_2 and Ag−TiO_2 nanofibers, X-ray powder diffraction was performed. The TiO_2 exhibits a mixed phase of anatase and rutile TiO_2 with well-defined diffraction peaks as shown in Figure 4, black. Characteristic peaks for the (101) phase of

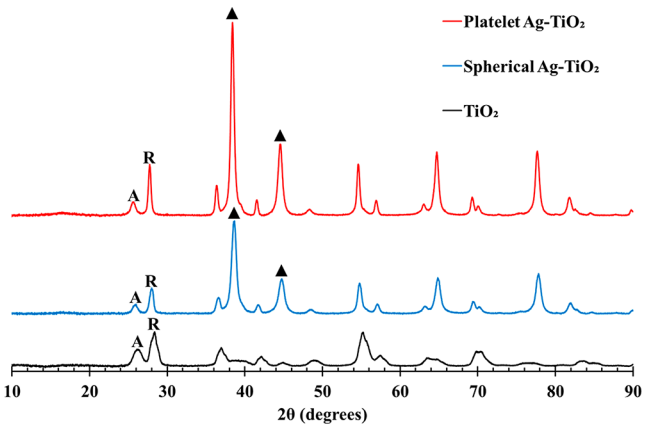

Figure 4. XRD spectra of TiO_2 (black), spherical Ag−TiO_2 (blue), and platelet Ag−TiO_2 (red). The major anatase (A) at 25.88° and rutile (R) at 28.04° peaks are labeled as well as the major peaks of (111) Ag at 38.66° and 44.74° (▲).

anatase were seen at 26.20° and the (110) phase of rutile at 28.36°. The weight fraction of the rutile phase was then calculated to be 72.2% and 27.8% anatase from the Scherrer equation, $W_R = 1/[1 + 0.8(I_A/I_R)]$, where I_A is the X-ray integrated intensity of the (101) reflection of anatase at 2θ of 26.20° and I_R is that of the (110) reflection of rutile at 2θ 28.36°.[50]

The XRD spectrum was also used to confirm the presence of the Ag on the surface of the TiO_2 nanofiber, while also confirming crystal form of the TiO_2 nanofiber, Figure 4, blue. For spherical Ag grown on a TiO_2 fiber, a mixed TiO_2 phase of (101) anatase (peak at 25.88°) and (110) rutile (peak at 28.04°) was observed. The (111) phase of Ag was clearly defined with two major peaks at 38.66° and 44.74°. However, when the crystal structure percentages of anatase and rutile were calculated at 77.0% rutile and 23.0% anatase, a slight deviation in comparison to its complementary sample without Ag. For the platelet Ag that was grown on TiO_2 nanofibers, Figure 4, red, a mixed TiO_2 phase crystal structure was again readily observed via the presence of the (101) anatase peak at 25.60° and the (110) rutile peak at 27.74°. Base treatment of the fibers and Ag synthesis again caused a deviation in the crystal structure percentages, increasing the rutile percentage, 82.5% rutile and 17.5% anatase composition. (111) Ag was again readily observable with major 2θ peaks at 38.4° and 44.56°. XPS analysis was further done to confirm the oxidation state of the Ag on the surface of TiO_2, Figure S8. The two 3d core levels $3d_{3/2}$ and $3d_{5/2}$ resulted in binding energies of 367.3 and 373.3 eV respectively. The difference of the peaks is 6 eV which corresponds to the presence of metallic silver. Although slightly shifted compared to values of bulk Ag^0 silver, this can be attributed to the migration of electrons to the TiO_2 signifying a covalent bond.[51,52]

Transient IR absorption spectroscopy was used in this study to probe for any free carriers generated from Ag−TiO_2 nanoplatelet composite fibers. The IR at 1900 cm^{-1} is transparent to any chemical groups, but sensitive to the change in the absorption of free carriers. Therefore, the transient IR absorption measures the absorption of free carriers inside the conduction band of TiO_2, following the 400 nm pump excitation of electron from its valence band. Figure 5

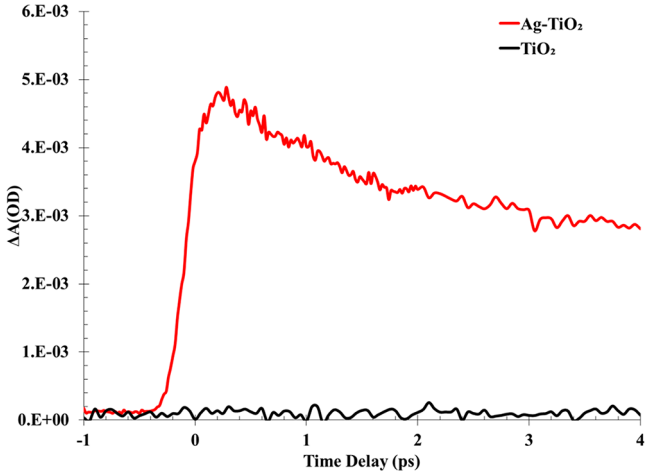

Figure 5. Transient IR spectroscopy of TiO_2 fibers (black) and TiO_2−Ag nanoplatelets composite fibers (red). Visible pump pulse of 400 nm with a pulse energy of 3 μJ and IR probe pulse of 5260 nm (1900 cm^{-1}) with a pulse energy of 1.5 μJ.

shows that no transient IR absorption occurred for the untreated TiO_2 (the blue curve). This suggests that the pump did not excite electrons from the valence band to the conduction band of the TiO_2 semiconductor alone. On the other hand, a prominent change in the transient IR absorption was observed for the sample in which Ag platelets were grown on the surface of the TiO_2 nanofibers (the red curve). To determine generation efficiency of free carriers as a function of

DOI: 10.1021/acs.jpcc.9b04026
J. Phys. Chem. C 2019, 123, 19579−19587

pump wavelength, visible pump−visible probe transient measurements were conducted using a range of discrete "pump" wavelengths including 515, 713, 742, 790, and 825 nm. The kinetic profiles of these experiments were probed at 600 nm, as provided in Figure 6. The negative change in

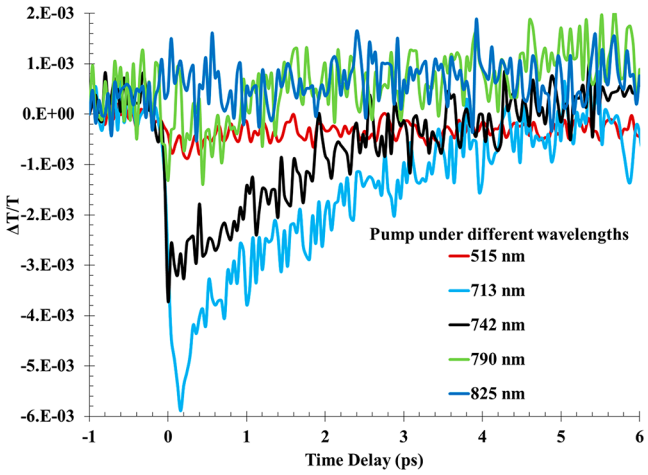

Figure 6. Kinetic profiles probing at 600 nm for anisotropic Ag−TiO_2 under different wavelength pump beams including 515, 713, 742, 790, and 825 nm. The greatest changes in transmission were observed for the scenarios in which the sample was pumped with 713 and 742 nm beams.

transmission at 600 nm is indicative of the newly generated free carriers. Moreover, the changes in transmission for the sample, when pumped with 713 and 742 nm, at t = 0, were significantly larger than for those pumped with other wavelengths (i.e., 515, 790, and 825 nm). These results are consistent with the fact that maximum free carrier generation was observed for those cases in which the incident radiation wavelength (713 and 742 nm) most closely matched the computational and experimental spectra of the silver nanoplatelets.

Finally, in order to elucidate the photocatalytic properties the Ag−TiO_2 composite fibers, all fibers in the study were exposed to methyl paraoxon in the presence of white, red, green, and blue LED irradiation, as well as in the dark (i.e., no direct source of irradiation). Our specific goal was to elucidate the impact of anisotropic silver on the photocatalytic properties of the composite fibers. Additionally, the impact of matching (or mismatching) the resonance exhibited by the nanoplatelets with the color of LED illumination was explored in the experiments. This was done to test our hypothesis that catalysis would be maximized when the resonance of the nanoplatelets most closely matched the wavelength band of the incident radiation.

Degradation of methyl paraoxon is reported as percent conversion of the absorbing nitrophenoxide product after 120 min of irradiation, Figure 7. Percent conversion as a function of time for each degradation experiment including untreated TiO_2, base-treated TiO_2, spherical Ag−TiO_2 and, platelet Ag−TiO_2 can be seen in Supporting Information, Figures S1−S4. In each experiment, the catalyst was stirred in the buffer solution, *N*-ethyl morpholine, 30 min prior to adding the methyl paraoxon. This was done to allow for the adsorption−desorption between the catalyst and the solution to equilibrate. At a pH of 10, a small percent conversion of methyl paraoxon will convert to nitrophenoxide is via base-catalyzed hydrolysis

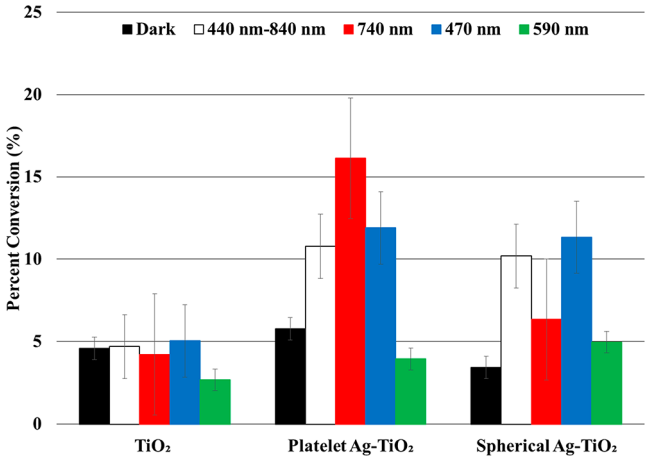

Figure 7. Graph depicting the LED source of irradiation versus the percent conversion of methyl paraoxon to nitro phenoxide at 120 min. Colors within the graph correspond to the color of the LED light source, white (440−840 nm), red (740 nm), blue (470 nm), and green (590 nm).

When TiO_2 was introduced to methyl paraoxon, the resulting percent conversions were all similar in the case of the dark versus the LED irradiation; this small percent conversion over the course of the experiment can be attributed to the background reaction between the methyl paraoxon and the buffer solution.[53] More notable results were obtained when methyl paraoxon was exposed to the composite Ag−TiO_2 nanofibers that contained either spherical or nanoplatelet silver nanoparticles. Upon inspection of computational and experimental results provided in Figure 3, 40 nm silver nanospheres typically absorb near 470 nm, while a distribution of silver nanoplatelets (with major dimensions that range from 40 to 75 nm) nominally absorb from 400 to 850 nm, with a maxima near 700 nm. With these facts in mind, a graph detailing the impact of irradiation color on the percent conversion of methyl paraoxon is provided in Figure 7.

Upon exposure to the white LED (440−840 nm), the blue LED (470 nm), the green LED (590 nm), and the red LED (740 nm), the catalytic results obtained for the platelet Ag−TiO_2 fibers and the spherical Ag−TiO_2 fibers are comparable. These results may be plausibly explained by the fact that (1) the resonance exhibited by the spherical Ag−TiO_2 overlaps with the illumination wavelength maxima of the white LED and the blue LED and (2) the broadband resonance of the platelet Ag−TiO_2 fibers overlaps with the illumination spectra of the white LED, the blue LED, and the green LED source. Conversely, in the presence of red LED light, a significant difference in catalytic efficiency was observed for the platelet Ag−TiO_2 fibers and the spherical Ag−TiO_2 fibers. Namely, the platelet Ag−TiO_2 fibers were much more efficient in degrading methyl paraoxon, in comparison to the spherical Ag−TiO_2 fibers. This efficiency may be understood in terms of the large population of the Ag nanodisks with plasmon peaks in the red spectral interval, as clearly demonstrated in Figure 3. Additionally, those Ag nanodisks with the "red" plasmons exhibit strong plasmonic extinction peaks. Hence, photochemistry is expected to be most efficient for the "red" excitation. Finally, the catalysis results for the platelet Ag−TiO_2 fibers are consistent with and complementary to the free carrier generation results obtained in Figure 6. Hot electron

DOI: 10.1021/acs.jpcc.9b04026
J. Phys. Chem. C 2019, 123, 19579−19587

generation was clearly maximized when the platelet Ag−TiO_2 fibers were "pumped" with red light (713 and 742 nm).

Upon inspection of Figure 7, it is evident that 100% conversion of methyl paraoxon was not achieved. However, the energy output of the LED sources must be considered when making any final conclusions, as the output power of all the LEDs was significantly less than that of the sun. Additionally, the absence of UV irradiation in this study significantly reduced the ability to generate electron−hole pairs within the TiO_2 itself, which have historically been used to catalytically breakdown a range of chemicals and agents. With these facts in mind, these results are very encouraging and demonstrate that the Ag−TiO_2 interaction improves catalytic ability in the visible region of the electromagnetic spectrum. More importantly, the catalytic breakdown of methyl paraoxon was maximized when the color spectrum of the LED, i.e., the red LED, overlapped with the strongest resonances exhibited by the silver nanoplatelet-TiO_2 composite.

6. CONCLUSIONS

In summary, a facile approach for growing anisotropic silver nanoparticles on the surface of TiO_2 nanofibers has been described. TEM and SEM imaging, experimental results, and computational modeling results support the presence of anisotropic silver nanoparticles on the surface of TiO_2 nanofibers. TEM images revealed a range of nanoplatelet sizes with major dimensions ranging from 40 to 75 nm. Computations indicate that silver nanoplatelets with these dimensions exhibit absorption maxima from 500 to 850 nm. This prediction was consistent with the experimental spectra of the Ag nanoplatelet−TiO_2 composite in which a maximum absorption near 700 nm was observed. Transient absorption and photocatalytic experiments revealed that when the plasmonic resonance of the platelets most closely matched the wavelength of incident radiation (713 nm for transient absorption and red LED for catalysis), maximum charge generation and catalytic breakdown of methyl paraoxon were achieved, respectively.

■ ASSOCIATED CONTENT

Supporting Information

The Supporting Information is available free of charge on the ACS Publications website at DOI: 10.1021/acs.jpcc.9b04026.

TGA, XPS, additional microscopy, additional degradation plots, LED spectra, energy measurements of LED sources, and quantum yield, given in Figures S1−S9 and Tables S1 and S2. (PDF)

■ AUTHOR INFORMATION

Corresponding Author

*(B.G.D.) Telephone: 410-436-5282. E-mail: brendan.g.delacy.civ@mail.mil.

ORCID

Hui Fang: 0000-0002-4024-1234
Xiang-Tian Kong: 0000-0002-8554-0369
Alexander O. Govorov: 0000-0003-1316-6758
Yi Rao: 0000-0001-9882-1314
Hai-Lung Dai: 0000-0001-6925-8075
Brendan G. DeLacy: 0000-0003-0648-4467

Notes

The authors declare no competing financial interest.

■ ACKNOWLEDGMENTS

We acknowledge funding by the department of the Army Basic Research Program, sponsored by the U.S Army Combat Capabilities Development Command Chemical Biological Center. A.O.G. and X.-T.K. were supported by an ARO Grant (Contract W911NF1920081) and the Volkswagen Foundation. This research was also funded by Reactive Chemical Systems Programs, U.S. Army Research Office (W911NF18020112)

■ REFERENCES

(1) Clavero, C. Plasmon-induced hot-electron generation at nanoparticle/metal-oxide interfaces for photovoltaic and photocatalytic devices. *Nat. Photonics* **2014**, *8* (2), 95−103.

(2) Mubeen, S.; Hernandez-Sosa, G.; Moses, D.; Lee, J.; Moskovits, M. Plasmonic Photosensitization of a Wide Band Gap Semiconductor: Converting Plasmons to Charge Carriers. *Nano Lett.* **2011**, *11* (12), 5548−5552.

(3) Christopher, P.; Ingram, D. B.; Linic, S. Enhancing Photochemical Activity of Semiconductor Nanoparticles with Optically Active Ag Nanostructures: Photochemistry Mediated by Ag Surface Plasmons. *J. Phys. Chem. C* **2010**, *114* (19), 9173−9177.

(4) Hou, W.; Cronin, S. B. A Review of Surface Plasmon Resonance-Enhanced Photocatalysis. *Adv. Funct. Mater.* **2013**, *23* (13), 1612−1619.

(5) Li, J.; Cushing, S. K.; Bright, J.; Meng, F.; Senty, T. R.; Zheng, P.; Bristow, A. D.; Wu, N. Ag@Cu2O Core-Shell Nanoparticles as Visible-Light Plasmonic Photocatalysts. *ACS Catal.* **2013**, *3* (1), 47−51.

(6) Kowalska, E.; Mahaney, O. O. P.; Abe, R.; Ohtani, B. Visible-light-induced photocatalysis through surface plasmon excitation of gold on titania surfaces. *Phys. Chem. Chem. Phys.* **2010**, *12* (10), 2344−2355.

(7) Méndez-Medrano, M. G.; Kowalska, E.; Lehoux, A.; Herissan, A.; Ohtani, B.; Rau, S.; Colbeau-Justin, C.; Rodríguez-López, J. L.; Remita, H. Surface Modification of TiO2 with Au Nanoclusters for Efficient Water Treatment and Hydrogen Generation under Visible Light. *J. Phys. Chem. C* **2016**, *120* (43), 25010−25022.

(8) Horiguchi, Y.; Kanda, T.; Torigoe, K.; Sakai, H.; Abe, M. Preparation of Gold/Silver/Titania Trilayered Nanorods and Their Photocatalytic Activities. *Langmuir* **2014**, *30* (3), 922−928.

(9) Grabowska, E.; Zaleska, A.; Sorgues, S.; Kunst, M.; Etcheberry, A.; Colbeau-Justin, C.; Remita, H. Modification of Titanium(IV) Dioxide with Small Silver Nanoparticles: Application in Photocatalysis. *J. Phys. Chem. C* **2013**, *117* (4), 1955−1962.

(10) Linic, S.; Christopher, P.; Ingram, D. B. Plasmonic-metal nanostructures for efficient conversion of solar to chemical energy. *Nat. Mater.* **2011**, *10* (12), 911−921.

(11) Cushing, S. K.; Li, J.; Bright, J.; Yost, B. T.; Zheng, P.; Bristow, A. D.; Wu, N. Controlling Plasmon-Induced Resonance Energy Transfer and Hot Electron Injection Processes in Metal@TiO2 Core−Shell Nanoparticles. *J. Phys. Chem. C* **2015**, *119* (28), 16239−16244.

(12) Ardo, S.; Meyer, G. J. Photodriven heterogeneous charge transfer with transition-metal compounds anchored to TiO2 semiconductor surfaces. *Chem. Soc. Rev.* **2009**, *38* (1), 115−164.

(13) Wu, K.; Chen, J.; McBride, J. R.; Lian, T. Efficient hot-electron transfer by a plasmon-induced interfacial charge-transfer transition. *Science* **2015**, *349* (6248), 632.

(14) Furube, A.; Du, L.; Hara, K.; Katoh, R.; Tachiya, M. Ultrafast Plasmon-Induced Electron Transfer from Gold Nanodots into TiO2 Nanoparticles. *J. Am. Chem. Soc.* **2007**, *129* (48), 14852−14853.

(15) Harutyunyan, H.; Martinson, A. B. F.; Rosenmann, D.; Khorashad, L. K.; Besteiro, L. V.; Govorov, A. O.; Wiederrecht, G. P. Anomalous ultrafast dynamics of hot plasmonic electrons in nanostructures with hot spots. *Nat. Nanotechnol.* **2015**, *10*, 770.

DOI: 10.1021/acs.jpcc.9b04026
J. Phys. Chem. C 2019, 123, 19579−19587

(16) Sykes, M. E.; Stewart, J. W.; Akselrod, G. M.; Kong, X.-T.; Wang, Z.; Gosztola, D. J.; Martinson, A. B. F.; Rosenmann, D.; Mikkelsen, M. H.; Govorov, A. O.; Wiederrecht, G. P. Enhanced generation and anisotropic Coulomb scattering of hot electrons in an ultra-broadband plasmonic nanopatch metasurface. *Nat. Commun.* **2017**, *8* (1), 986.
(17) Zhang, H.; Govorov, A. O. Optical Generation of Hot Plasmonic Carriers in Metal Nanocrystals: The Effects of Shape and Field Enhancement. *J. Phys. Chem. C* **2014**, *118* (14), 7606−7614.
(18) Besteiro, L. V.; Kong, X.-T.; Wang, Z.; Hartland, G.; Govorov, A. O. Understanding Hot-Electron Generation and Plasmon Relaxation in Metal Nanocrystals: Quantum and Classical Mechanisms. *ACS Photonics* **2017**, *4* (11), 2759−2781.
(19) Hartland, G. V.; Besteiro, L. V.; Johns, P.; Govorov, A. O. What's so Hot about Electrons in Metal Nanoparticles? *ACS Energy Letters* **2017**, *2* (7), 1641−1653.
(20) Gaya, U. I.; Abdullah, A. H. Heterogeneous photocatalytic degradation of organic contaminants over titanium dioxide: A review of fundamentals, progress and problems. *J. Photochem. Photobiol., C* **2008**, *9* (1), 1−12.
(21) Linsebigler, A. L.; Lu, G.; Yates, J. T. Photocatalysis on TiO_2 Surfaces: Principles, Mechanisms, and Selected Results. *Chem. Rev.* **1995**, *95* (3), 735−758.
(22) Awazu, K.; Fujimaki, M.; Rockstuhl, C.; Tominaga, J.; Murakami, H.; Ohki, Y.; Yoshida, N.; Watanabe, T. A Plasmonic Photocatalyst Consisting of Silver Nanoparticles Embedded in Titanium Dioxide. *J. Am. Chem. Soc.* **2008**, *130* (5), 1676−1680.
(23) Xin, B.; Jing, L.; Ren, Z.; Wang, B.; Fu, H. Effects of Simultaneously Doped and Deposited Ag on the Photocatalytic Activity and Surface States of TiO2. *J. Phys. Chem. B* **2005**, *109* (7), 2805−2809.
(24) Georgekutty, R.; Seery, M. K.; Pillai, S. C. A Highly Efficient Ag-ZnO Photocatalyst: Synthesis, Properties, and Mechanism. *J. Phys. Chem. C* **2008**, *112* (35), 13563−13570.
(25) Choi, J.; Park, H.; Hoffmann, M. R. Effects of Single Metal-Ion Doping on the Visible-Light Photoreactivity of TiO2. *J. Phys. Chem. C* **2010**, *114* (2), 783−792.
(26) Wolfe, D. B.; Oldenburg, S. J.; Westcott, S. L.; Jackson, J. B.; Paley, M. S.; Halas, N. J. Photodeposition of Molecular Layers on Nanoparticle Substrates. *Langmuir* **1999**, *15* (8), 2745−2748.
(27) Westcott, S. L.; Oldenburg, S. J.; Lee, T. R.; Halas, N. J. Construction of simple gold nanoparticle aggregates with controlled plasmon−plasmon interactions. *Chem. Phys. Lett.* **1999**, *300* (5−6), 651−655.
(28) Porter, L. A.; Ji, D.; Westcott, S. L.; Graupe, M.; Czernuszewicz, R. S.; Halas, N. J.; Lee, T. R. Gold and Silver Nanoparticles Functionalized by the Adsorption of Dialkyl Disulfides. *Langmuir* **1998**, *14* (26), 7378−7386.
(29) Pham, T.; Jackson, J. B.; Halas, N. J.; Lee, T. R. Preparation and Characterization of Gold Nanoshells Coated with Self-Assembled Monolayers. *Langmuir* **2002**, *18* (12), 4915−4920.
(30) Banholzer, M. J.; Osberg, K. D.; Li, S.; Mangelson, B. F.; Schatz, G. C.; Mirkin, C. A. Silver-Based Nanodisk Codes. *ACS Nano* **2010**, *4* (9), 5446−5452.
(31) Hurst, S. J.; Lytton-Jean, A. K. R.; Mirkin, C. A. Maximizing DNA Loading on a Range of Gold Nanoparticle Sizes. *Anal. Chem.* **2006**, *78* (24), 8313−8318.
(32) Millstone, J. E.; Georganopoulou, D. G.; Xu, X.; Wei, W.; Li, S.; Mirkin, C. A. DNA-Gold Triangular Nanoprism Conjugates. *Small* **2008**, *4* (12), 2176−2180.
(33) Miller, O. D.; Hsu, C. W.; Reid, M. T. H.; Qiu, W.; DeLacy, B. G.; Joannopoulos, J. D.; Soljačić, M.; Johnson, S. G. Fundamental Limits to Extinction by Metallic Nanoparticles. *Phys. Rev. Lett.* **2014**, *112* (12), 123903.
(34) Sherry, L. J.; Chang, S.-H.; Schatz, G. C.; Van Duyne, R. P.; Wiley, B. J.; Xia, Y. Localized Surface Plasmon Resonance Spectroscopy of Single Silver Nanocubes. *Nano Lett.* **2005**, *5* (10), 2034−2038.
(35) Xia, Y.; Halas, N. J. Shape-Controlled Synthesis and Surface Plasmonic Properties of Metallic Nanostructures. *MRS Bull.* **2005**, *30* (5), 338−348.
(36) Wiley, B. J.; Im, S. H.; Li, Z.-Y.; McLellan, J.; Siekkinen, A.; Xia, Y. Maneuvering the Surface Plasmon Resonance of Silver Nanostructures through Shape-Controlled Synthesis. *J. Phys. Chem. B* **2006**, *110* (32), 15666−15675.
(37) Katz, M. J.; Mondloch, J. E.; Totten, R. K.; Park, J. K.; Nguyen, S. T.; Farha, O. K.; Hupp, J. T. Simple and Compelling Biomimetic Metal−Organic Framework Catalyst for the Degradation of Nerve Agent Simulants. *Angew. Chem., Int. Ed.* **2014**, *53* (2), 497−501.
(38) Raushel, F. M. Catalytic detoxification. *Nature* **2011**, *469*, 310.
(39) Rastogi, V. K.; Defrank, J. J.; Cheng, T.-c.; Wild, J. R. Enzymatic Hydrolysis of Russian-VX by Organophosphorus Hydrolase. *Biochem. Biophys. Res. Commun.* **1997**, *241* (2), 294−296.
(40) Kim, K.; Tsay, O. G.; Atwood, D. A.; Churchill, D. G. Destruction and Detection of Chemical Warfare Agents. *Chem. Rev.* **2011**, *111* (9), 5345−5403.
(41) Liu, J.; McCarthy, D. L.; Cowan, M. J.; Obuya, E. A.; DeCoste, J. B.; Skorenko, K. H.; Tong, L.; Boyer, S. M.; Bernier, W. E.; Jones, W. E., Jr Photocatalytic activity of TiO2 polycrystalline sub-micron fibers with variable rutile fraction. *Appl. Catal., B* **2016**, *187*, 154−162.
(42) Mahshid, S.; Askari, M.; Ghamsari, M. S. Synthesis of TiO2 nanoparticles by hydrolysis and peptization of titanium isopropoxide solution. *J. Mater. Process. Technol.* **2007**, *189* (1−3), 296−300.
(43) Su, C.; Liu, L.; Zhang, M.; Zhang, Y.; Shao, C. Fabrication of Ag/TiO2 nanoheterostructures with visible light photocatalytic function via a solvothermal approach. *CrystEngComm* **2012**, *14* (11), 3989−3999.
(44) Alahmad, A.; Eleoui, M.; Falah, A.; Alghoraibi, I. Preparation of colloidal silver nanoparticles and structural characterization. *Phys. Sci. Res. Int.* **2013**, *1*, 89−96.
(45) Fang, H.; Wu, Y.; Kuhn, D. L.; Zander, Z.; DeLacy, B. G.; Rao, Y.; Dai, H.-L. Electron injection from a carboxylic anchoring dye to TiO_2 nanoparticles in aprotic solvents. *Chem. Phys.* **2018**, *512*, 93−97.
(46) Johnson, P. B.; Christy, R. W. Optical Constants of the Noble Metals. *Phys. Rev. B* **1972**, *6* (12), 4370−4379.
(47) Mudunkotuwa, I. A.; Grassian, V. H. Citric Acid Adsorption on TiO_2 Nanoparticles in Aqueous Suspensions at Acidic and Circumneutral pH: Surface Coverage, Surface Speciation, and Its Impact on Nanoparticle−Nanoparticle Interactions. *J. Am. Chem. Soc.* **2010**, *132* (42), 14986−14994.
(48) Ahmed, S.; Rasul, M. G.; Martens, W. N.; Brown, R.; Hashib, M. A. Advances in Heterogeneous Photocatalytic Degradation of Phenols and Dyes in Wastewater: A Review. *Water, Air, Soil Pollut.* **2011**, *215* (1), 3−29.
(49) Li, Y.-F.; Selloni, A. Pathway of Photocatalytic Oxygen Evolution on Aqueous TiO2 Anatase and Insights into the Different Activities of Anatase and Rutile. *ACS Catal.* **2016**, *6* (7), 4769−4774.
(50) Patterson, A. L. The Scherrer Formula for X-Ray Particle Size Determination. *Phys. Rev.* **1939**, *56*, 978−982.
(51) Lee, S.-W.; Obregón, S.; Rodríguez-González, V. The role of silver nanoparticles functionalized on TiO2 for photocatalytic disinfection of harmful algae. *RSC Adv.* **2015**, *5* (55), 44470−44475.
(52) Kumar, R.; Rashid, J.; Barakat, M. A. Zero valent Ag deposited TiO_2 for the efficient photocatalysis of methylene blue under UV-C light irradiation. *Colloids and Interface Science Communications* **2015**, *5*, 1−4.
(53) McCarthy, D. L. *Fabrication of Electrospun TiO_2/Polymer Composite Nanofibers For Photocatalysis and Degradation of Toxins*. Thesis; Binghamton University: 2016.

DOI: 10.1021/acs.jpcc.9b04026
J. Phys. Chem. C 2019, 123, 19579−19587